Study of structural, optical, and paramagnetic properties of $Zn_{1-x}Co_xS$ nanoparticles prepared via co-precipitation

V. V. Jadhavar[1,*] , V. D. Mote[1], and B. S. Munde[2,*]

[1] Thin Films and Materials Science Research Laboratory, Department of Physics, Dayanand Science College, Latur 413512, Maharashtra, India
[2] Department of Physics, K.K.M. College, Manwath, Maharashtra, India

ABSTRACT

Co-doped ZnS ($Zn_{1-x}Co_xS$) nanoparticles were successfully synthesized by the chemical co-precipitation method. X-ray diffraction (XRD) patterns showed that nanoparticles were polycrystalline in nature with the cubic crystal structure. A reduction in the lattice parameter for Co-doped ZnS nanoparticles was observed, indicating that Co^{2+} ions are incorporated into the ZnS matrix. The average crystallite size of prepared nanoparticles calculated using Scherrer's formula and found to be 2–3 nm. The crystallite size and microstrain of samples were investigated by the W–H analysis method. EDX spectra of doped samples confirmed the presence of the elements Zn, S, and Co. The field emission-scanning electron microscope (FE-SEM) images of nanoparticles are spherical with agglomeration. UV–visible measurements revealed that the optical band-gap of $Zn_{1-x}Co_xS$ nanoparticles decreased with increasing cobalt concentration. Magnetic properties showed a paramagnetic-like behavior in all samples prepared at room temperature.

1 Introduction

Semiconductor nanoparticles have attractive materials due to their potential applications in nanospintronic devices [1–3]. Nanoparticles have undergone significant changes in the structure, optical, and magnetic properties due to the large surface area to the volume ratio and quantum confinement of the material [4–6]. Among the II–VI semiconductors, zinc sulfide (ZnS) is an important material because of a wide bandgap of 3.67 eV at 300 K, 40 meV as an exciton binding energy and good chemical stability [7]. Moreover, ZnS is also very promising material used in some applications such as lasers, displays, and sensors [8–10]. Recently, optical and magnetic properties of ZnS nanoparticles have changed, when the transition metals such as Fe, Ni, and Mn doped [11–13].

Beside these nanoparticles, Co^{2+}-doped ZnS nanoparticles are of special interest due to their

Address correspondence to E-mail: jadhavarvikas@gmail.com; bhaskarmunde@yahoo.com

attractive unique properties for applications in light-emitting diodes, lasers, sensors, bio-devices, infrared windows, flat panel displays, phosphors, etc. [14–17]. Saikia et al. [18] reported ferromagnetism in ZnS nanocrystals and the effect of Co concentration was investigated. Pathak et al. [19] studied the optical properties of cobalt-doped ZnS nanophosphors through the chemical co-precipitation method and found a blue shift of the bandgap due to the quantum confinement effect. Room temperature magnetic properties has been observed in Co-doped ZnS samples and magnetization also decreases with increased concentration of Co which was reported by Sambasivam et al. [20]. Kumar et al. [21] found room temperature ferromagnetism in Ni-doped ZnS nanoparticles. Eryong et al. [22] observed superparamagnetism in the Fe-doped ZnS nanoparticles. According to the reported literature survey, transition metal-doped ZnS materials are room temperature magnetism in DMS that is still the subject of debate. Hence, we have prepared Co-doped ZnS nanoparticles and investigated the optical and magnetic properties.

This paper contains the synthesis of undoped and Co-doped ZnS nanoparticles by the chemical co-precipitation technique. This technique is used because it is a low cost and the dopant concentration can be easily attained [2]. The structural, compositional, morphological, optical, and magnetic properties of the prepared nanoparticles were carried out by X-ray diffraction (XRD), energy-dispersive X-ray analyser (EDS), field emission-scanning electron microscope (FE-SEM), UV–Visible spectroscopy (UV–Vis), and vibrating sample magnetometer (VSM). The optical and magnetic studies of mentioned nanoparticles are discussed in detail.

2 Experimental

2.1 Synthesis of $Zn_{1-x}Co_xS$ nanoparticles

$Zn_{1-x}Co_xS$ (x = 0.00, 0.02, 0.04, and 0.06) nanoparticles were prepared at room temperature using a co-precipitation method. Zinc acetate dehydrates [$Zn(CH_3COO)_2 \cdot 2H_2O$], cobalt nitrate [$Co(NO_3)_3 \cdot 9H_2O$], and sodium sulfide [$Na_2S \cdot H_2O$] were the reactants used in the experiment. These reactants are respectively the source materials for zinc, cobalt, and sulfur. Double distilled water was used as a solvent.

All the chemicals used in the process of synthesis are of an analytical reagent grade (Merck chemicals, INDIA). The synthesis process is as follows: Zinc acetate dehydrates and cobalt nitrate are weighed according to the stoichiometric ratio. These two reactants are then separately dissolved into 100 ml of water to prepare 1 M of solution. Similarly, a sodium sulfide solution of 1 M is being prepared. These solutions are continuously stirred in separate beakers using a magnetic stirrer for 1 h to obtain a clear solution. Then, the solution of 1 M cobalt nitrate was added drop-wise to the solution of 1 M zinc acetate which was kept on stirring. The mixture is added drop-wise to 1 M of sodium sulfide with continuous vigorous stirring. The stirring was continued for 2 h until the fine precipitates were formed. Precipitate containing cobalt-doped ZnS nanoparticles have been filtered out using Whatman paper to extract the sodium impurities. The wet precipitate is washed with distilled water several times and remaining water after washing was removed with several washings of ethanol. The prepared samples were dried for 24 h at room temperature, and then kept for 8 h in an oven at 80 °C to remove the moisture. Finally, using a mortar pester, the dried samples were crushed to a fine powder. The prepared powder samples are then used to study their structural, morphological, compositional, optical, and magnetic properties. The same process is used in the preparation of pure ZnS nanoparticles without doping the material.

2.2 Characterization techniques

The $Zn_{1-x}Co_xS$ nanoparticles were characterized using various techniques. The structural studies were performed using an X-ray diffractometer (REGACO ULTIMA-4). Field emission-scanning electron microscope (FE-SEM) with an energy-dispersive X-ray analyser (EDS) attachment (Model: CARL ZEISS Sigma IV) was used to perform chemical analysis. The optical absorption spectra were observed by a UV–visible spectrometer (JASCO V730) for measuring the absorption characteristics. A vibrating sample magnetometer (VSM) (Lakeshore-7404) was used to measure the magnetization characteristics of the prepared samples.

3 Results and discussion

3.1 Structural studies

Figure 1 shows X-ray diffraction patterns of Zn_{1-x}-Co_xS nanoparticles. All peaks correspond to reflection from the (111), (220), and (311) planes of cubic ZnS with the polycrystalline nature of all nanoparticles. Diffraction peaks of all the samples are in good agreement with the standard JCPDS card no. 03-0570. The Co-doped ZnS nanoparticles are also polycrystalline nature and fit well with the cubic ZnS crystal. It is interesting to note that the cubic crystal structure of Co-doped samples have been unchanged up to 6% Co doping concentration. Pathak et al. [23] observed similar behavior for XRD patterns of Co-doped ZnS nanoparticles. No impurity peaks corresponding to cubic ZnS or cobalt compounds were observed, demonstrating that prepared nanoparticles are single phase. The broadening of the diffraction peaks, however, indicates that the particles are in extremely small nanosizes. Interestingly, the intensity of reflection planes increases in Co-doped nanoparticles as compared to ZnS nanoparticles indicated Co doping concentration to affect.

XRD patterns were analyzed to estimate the structural parameters such as lattice constant, crystallite size, lattice strain, and dislocation density. The lattice constant has been calculated using the following relationship:

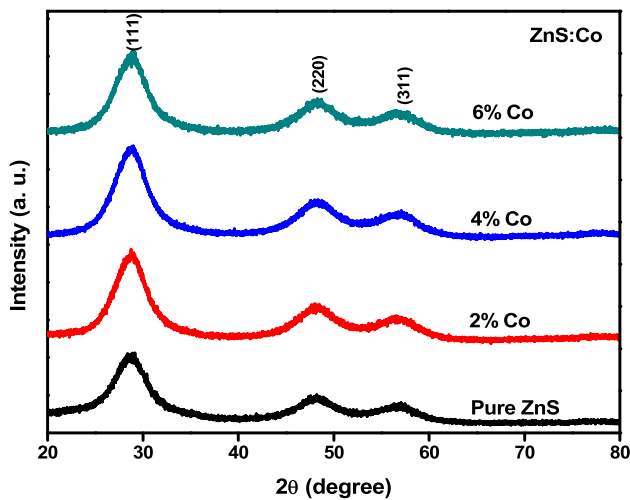$$a = \frac{\lambda}{2 \sin \theta} \sqrt{h^2 + k^2 + l^2} \tag{1}$$

Fig. 1 XRD patterns of $Zn_{1-x}Co_xS$ nanoparticles

where λ is the X-ray wavelength (0.15406 nm), θ is the diffraction angle, and (h, k, l) is miller indices of the crystal plane. The value of the lattice constant is calculated and listed in Table 1. It is found that with Co doping concentration, there is decrease in lattice constant of ZnS nanoparticles. Similar type of behavior is also reported by Salem et al. [24] for Co-doped ZnS nanoparticles. The decrease in the lattice constant may be attributed to the small ionic radius of Co^{+2} (0.072 nm) as compared to the Zn^{2+} (0.074 nm). Furthermore, the cell volume of the ZnS nanoparticles decreases with an increase in the Co doping concentration (seen in Table 1). The significant change in lattice constant and volume of unit cell of the ZnS host materials further signifies the successful doping of Co foreign atoms.

The crystallite size (D) is determined using the Debye–Scherrer equation:

$$D = \frac{K\lambda}{\beta \cos \theta} \tag{2}$$

where D is the mean crystallite size, K is particle shape factor (0.9), λ is the wavelength of X-rays used, θ is the angle of diffraction, and β represents the integral breadth obtained after the instrumental correction has been applied as

$$\beta = (\beta_m^2 - \beta_i^2)^{1/2} \tag{3}$$

where β_i is the instrumental broadening measured using the standard silicon sample and β_m is the observed integral breadth of the XRD peaks of samples [25, 26]. The average crystallite size of the nanoparticles is found to be in the range of 2–3 nm as shown in Table 1. The crystallite sizes were varied as the Co doping was increased, which is in good agreement with the previous result reported by Sambasivam et al. [27]. This is attributed to the replacement of Zn^{2+} ions by Co^{2+} ions during the formation of the Co-doped ZnS nanoparticles. Microstrain (ε) [28] and dislocation density (δ) [29] for all nanoparticles are calculated using the following equations:

$$\varepsilon = \frac{\beta \cos \theta}{4} \tag{4}$$

$$\delta = \frac{1}{D^2} \tag{5}$$

Here, D is the average crystallite size (nm). The microstrain and dislocation density of the prepared

Table 1 Structural parameters of $Zn_{1-x}Co_xS$ nanoparticles

Sample Co doping	Lattice constant (Å)	Unit cell volume (Å)^3	D (nm)	Microstrain $\varepsilon \times 10^{-3}$	Dislocation density (Line/m^2)	D_{W-H} (nm)	Microstrain W–H $\varepsilon \times 10^{-3}$
0.00	5.3814	155.84	2.0888	16.72	0.229	2.39	15.91
0.02	5.3718	155.01	2.0806	16.71	0.231	3.09	27.70
0.04	5.3687	154.74	2.0471	16.99	0.238	3.77	32.28
0.06	5.3628	154.23	2.0922	16.61	0.228	4.24	36.07

nanoparticles are listed in Table 1. It is seen that the microstrain of nanoparticles increases with an increasing concentration of Co doping. It may be due to the doping of the Co. Moreover, the dislocation density of nanoparticles increases with an increase in Co doping, while average crystallite size of the nanoparticles decreases with an increase in Co doping concentration. It means that the dislocation density of the prepared nanoparticles is inversely proportional to size of crystallite. This indicates that the crystallinity of the ZnS samples with Co doping is reduced.

3.2 Estimation of crystallite size and microstrain from Williamson–Hall plot

The crystallite size and microstrain of the nanoparticles can be calculated by the Williamson–Hall (W–H) equation [30]:

$$\beta \cos \theta = K\lambda/D + 4\varepsilon \sin \theta \qquad (6)$$

where β is the FWHM in radian, θ is the angle of diffraction, $K = 0.9$ is a constant shape factor for spherical nanoparticles, $\lambda = 1.5406$ Å is the wavelength of Cu-Kα radiation, D is the average crystallite size, and ε is the microstrain induced. By plotting $\beta\cos\theta$ along the y-axis and $4\sin\theta$ along the x-axis, the average crystallite size and strain induced in the lattice were determined. The W–H equation indicates that factor $K\lambda/D$ is the intercept and ε is the slope of the line when compared to the general equation of line $y = mx + c$ where m is the slope and c is the intercept. Thus, from the intercept, the value of the average crystallite size can be obtained, while the strain induced can be determined from the slope of the line. Figure 2 shows the W–H plot of $Zn_{1-x}Co_xS$ nanoparticles. For different concentrations of Co in ZnS, the estimated values of average crystallite size

from W–H plots and the respective strains are given in Table 1. The average crystallite size obtained from W–H plots is 2–5 nm and was well compatible with Scherrer formula values. It is observed that the average crystallite size and microstrain calculated from Scherrer's equation and W–H method in the doped nanoparticles do not change systematically with Co doping concentration, which may be due to the lattice disorder formed in the nanoparticles at higher doping concentrations due to the small difference in the ionic radii of Co^{2+} ions and Zn^{2+}ions.

3.3 Morphological studies

Figure 3a–d shows Field emission-scanning electron microscope (FE-SEM) of $Zn_{1-x}Co_xS$ nanoparticles. It can be seen from Fig. 3a that the grain size around 50 nm is grown with the non-uniform distribution. As Co doping increased to 6%, more number of grains is found as compared to the ZnS sample as shown in Fig. 3b–d. However, it can also notice that high agglomeration among smaller crystallites to form grains increases with increasing in Co doping concentration. The enhanced agglomeration of Co-doped ZnS nanoparticles is due to the higher relative surface area along with a higher relative number of surface atoms, nanoparticles attempt to make bonds that appear to form between adjacent particles. Nanoparticles with Co doping concentration are also shown spherical-like structure due to small grains. It implies that morphological properties are independent of Co doping concentration. Also, no doping-based morphological features were observed [31].

3.4 Elemental analysis

Elemental dispersive X-ray analysis verified that cobalt was incorporated into ZnS lattice. Figure 4 shows the EDX spectra of $Zn_{1-x}Co_xS$ nanoparticles.

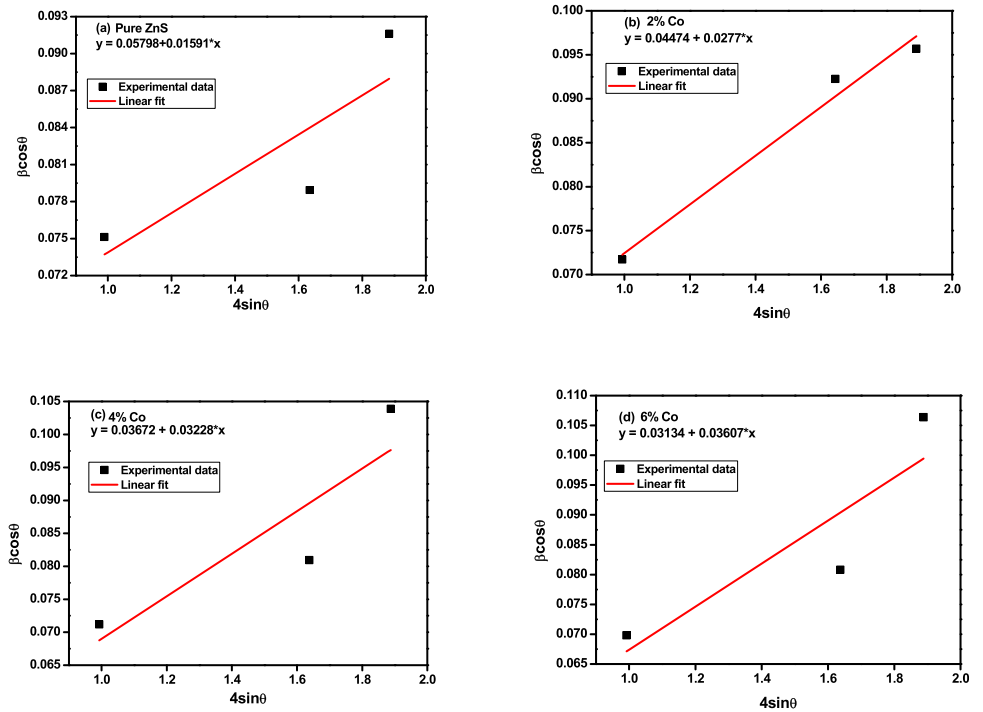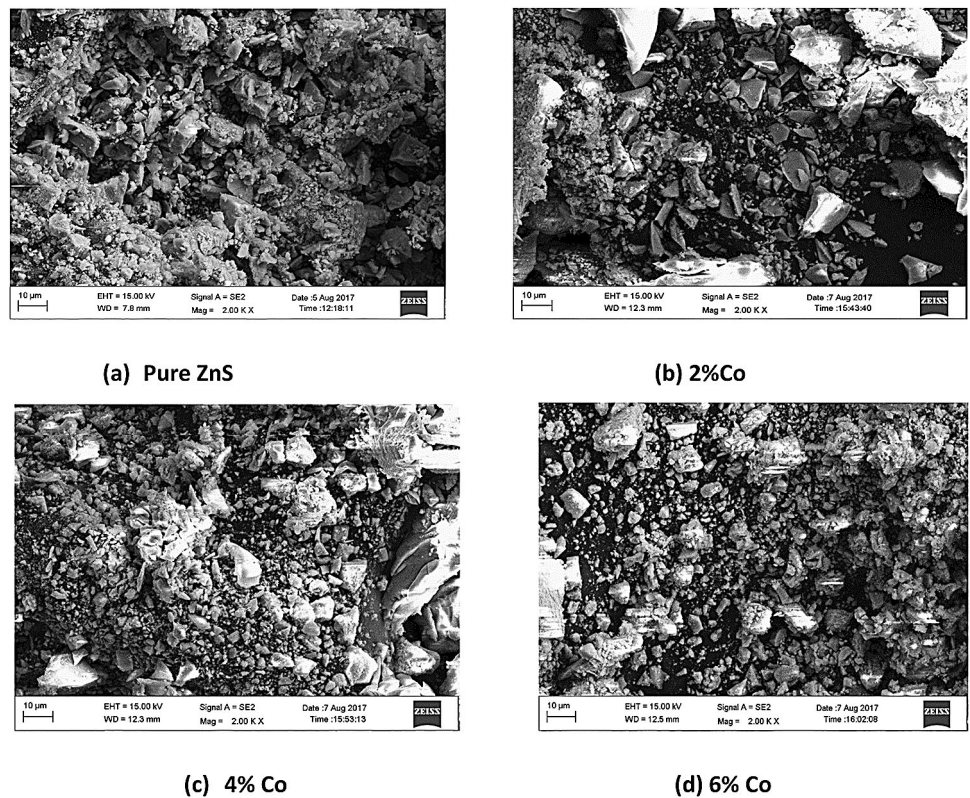**Fig. 2** Williamson–Hall plots of $Zn_{1-x}Co_xS$ nanoparticles

(a) Pure ZnS
y = 0.05798+0.01591*x

(b) 2% Co
y = 0.04474 + 0.0277*x

(c) 4% Co
y = 0.03672 + 0.03228*x

(d) 6% Co
y = 0.03134 + 0.03607*x

Fig. 3 FE-SEM images of $Zn_{1-x}Co_xS$ nanoparticles
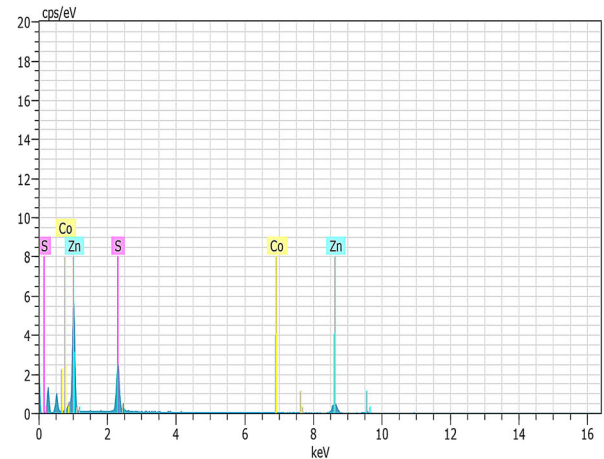

(a) Pure ZnS

(b) 2%Co

(c) 4% Co

(d) 6% Co

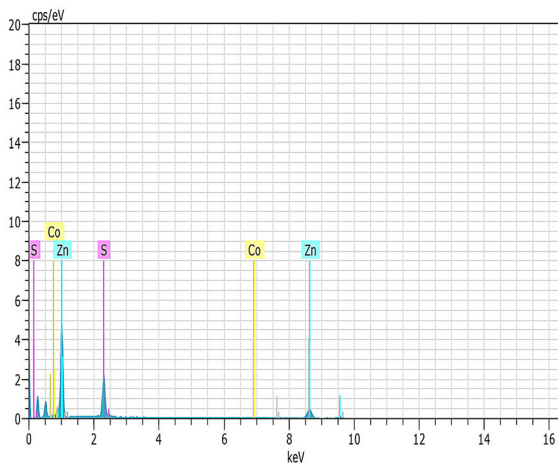The spectra reveal that the Zn and S elements are present in pure ZnS, while the Zn, S, and Co elements are present in the doped samples. The observed amount of Co in 2, 4, and 6% Co-doped samples are 0.12, 1.45, and 2.98%, respectively, and listed in Table 2. This indicates that the observed amount is
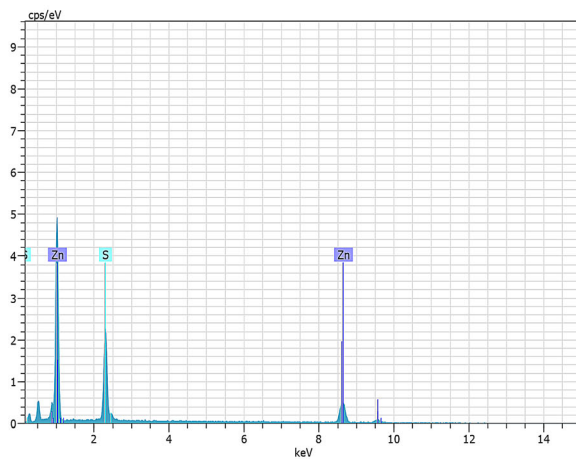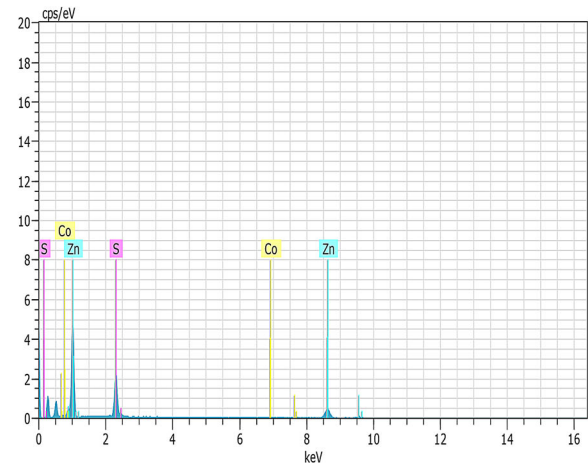
(a) Undoped ZnS

(b) 2% Co

(c) 4% Co

(d) 6% Co

Fig. 4 EDX spectra of $Zn_{1-x}Co_xS$ nanoparticles

less as compared to the actual doped amount. It may be due to excessive washing of samples leading to a decrease in the observed percentage of doped cobalt. From the EDX spectra study, it also confirms that the atomic weight percentage of cobalt increased with increasing cobalt content. It means that cobalt surely enters into ZnS lattice.

3.5 Optical studies

Figure 5 shows the UV–vis absorbance spectra of $Zn_{1-x}Co_xS$ nanoparticles at room temperature. From the figure, it is observed that absorbance increased

Table 2 Elements composition analysis of Co-doped ZnS samples

Elements	Atomic%			
	0% Co	2% Co	4% Co	6% Co
Zn	69.24	64.82	66.51	64.95
S	30.76	35.06	32.04	32.07
Co	00.00	0.12	1.45	2.98
Total	100	100	100	100

with increasing Co doping. According to the reported literature, the absorbance also depends upon some factors such as particle size, deficiency, defects in

grain structure [32]. In our case, absorbance peak moves toward larger wavelengths due to increase in number of structural defects with increasing Co content.

The relation between the incident photon energy (hν) and the absorption coefficient (α) is given by Wood and Tauc's equation:

$$(\alpha h v)^{1/n} = A(h v - E_g) \tag{7}$$

where A is constant, h is Planck's constant, v is photon frequency, and E_g is the energy bandgap of the material, and exponent n depends on the type of transition. For direct allowed transition, $n = 1/2$, indirect allowed transition, $n = 2$, direct forbidden, $n = 3/2$ and indirect forbidden, $n = 3$. Figure 6 shows the Tauc plot of $Zn_{1-x}Co_xS$ nanoparticles. The linear nature of the graph represents the presence of a direct transition. The bandgap energy of the samples is calculated by plotting $(\alpha h v)^2$ versus $h v$. The linear fitting of the straight portion of the curve on the $h v$ axis gives the value of energy bandgap. For the samples $x = 0.00, 0.02, 0.04,$ and 0.06, $Zn_{1-x}Co_xS$ nanoparticles have bandgap values 3.33, 2.92, 2.81, and 2.71 eV, respectively. The reduction in bandgaps of prepared nanoparticles can be attributed to amount of defects (strain) in nanoparticles. This fact is supported by the values of microstrain that are calculated from the XRD data. Figure 7 shows dependence of ln (α) of undoped and Co-doped ZnS nanoparticles upon the photon energy from which the Urbach energy can be obtained. The Urbach energy of the samples $x = 0.00, 0.02, 0.04,$ and 0.06 have values 0.269, 0.274, 0.311, and 0.528 eV, respectively, and represents amount of defects in the material [33, 34]. Thus it is clear that defects are
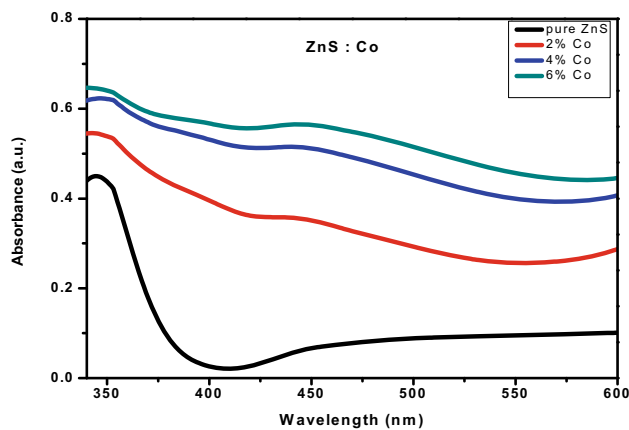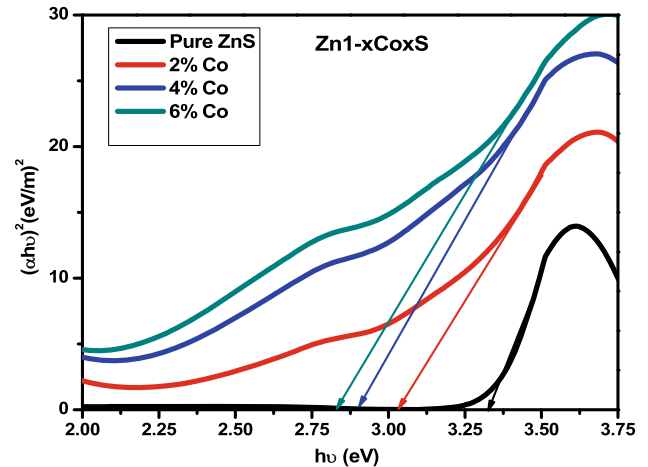

Fig. 6 Tauc plot of $Zn_{1-x}Co_xS$ nanoparticles

responsible for the variation in bandgap value. Figure 8 shows the variation of bandgap with doping concentration of cobalt and found the optical bandgap decrease with increasing Co content. Patel et al. predicted that the reduction in the bandgap for Co-doped ZnS nanoparticles might be due to the sp-d exchange interaction between the band electrons and the localized d electrons of Co^{2+} ions [35]. Hence, Co-doped ZnS nanoparticles prepared by the co-precipitation method exhibited excellent properties for a myriad of practical applications.

3.6 Magnetic studies

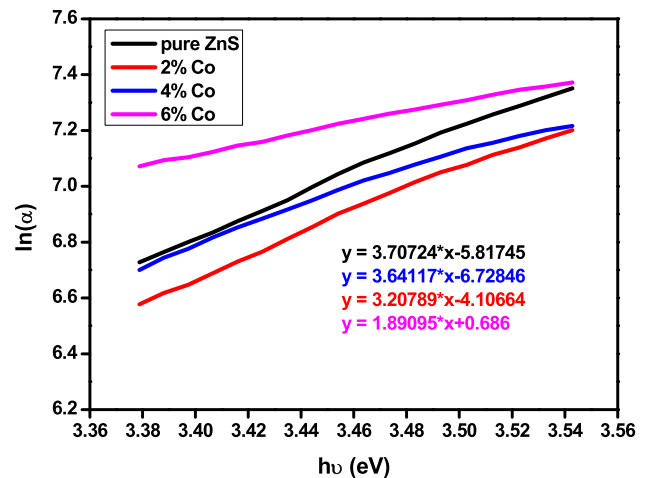The magnetic behavior of Co-doped ZnS nanoparticles with varying doping concentrations was

Fig. 7 Dependence of ln (α) of undoped and Co-doped ZnS nanoparticles upon the photon energy from which the Urbach energy can be obtained

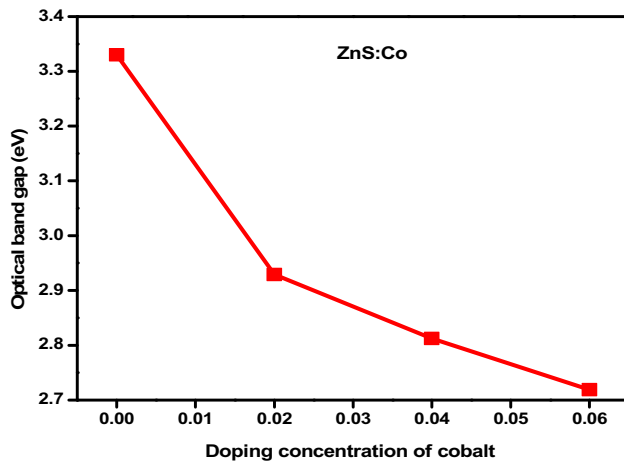**Fig. 5** Absorption spectra of $Zn_{1-x}Co_xS$ nanoparticles

Fig. 8 Variation of E_g with doping concentration of cobalt

measured at 300 K by VSM using a magnetic field (H) of 5 kOe. Magnetization versus applied magnetic field (M–H) curves for undoped and Co-doped ZnS nanoparticles at room temperature are shown in Fig. 9a–d, respectively. The undoped ZnS sample exhibits M-H curve which appears to be linear with a positive slope and represents paramagnetic behavior, because of surface vacancies and small crystallite size of the nanoparticles. Figure 9b–d shows the M–H curves for 2%, 4%, and 6% Co-doped ZnS nanoparticles at room temperature. However, the M–H curves for doped samples are also linear with a positive slope indicate the presence of a paramagnetic-like behavior at room temperature. Saikia et al. [36] reported that room temperature ferromagnetism arises in undoped ZnS due to surface vacancy states. Kumar et al. [13] revealed that superparamagnetic-like behavior in pure ZnS and 1% Ni-doped ZnS nanocrystals could be attributed to the extremely small particle size ∼ 2.9 nm of prepared nanocrystals. Our result is in good agreement with the studies by Elsi et al. [37] and predicted smaller nanoparticles (< 10 nm) are the root cause of superparamagnetism in Co-doped ZnS nanoparticles. Furthermore, the M–H curves of undoped and Co-doped ZnS nanoparticles represent the presence of paramagnetic contributions to the magnetization. It may be due to the presence of prepared nanoparticles of extremely small size and Co doping. A paramagnetic contribution was observed in Co-doped ZnO nanoparticles because some of the nanoparticles may be in the superparamagnetic regime or that some of the cobalt ions are weakly coupled or not interagent among

themselves has been reported by Franco Jr et al. [38]. The change in the magnetic properties of Co-doped ZnS nanoparticles might be attributed to the structural and morphological changes that occurred due to the Co doping. A decrease in the crystallite size of the nanostructure material leads to an increase in magnetic performance. The result suggests that the Co-doped ZnS nanoparticles show good paramagnetic properties at room temperature. Bi et al. [39] reported room temperature ferromagnetism in Co-doped ZnS and found that gradually becomes weak with the increase of Co doping concentration due to the sulfur vacancies in the ZnS lattice. Wu et al. [40] observed that the pure ZnS samples were superparamagnetic, whereas the doped samples exhibit ferromagnetism mainly due to the substitution of Ni^{2+} on Zn^{2+} sites not due to Ni cluster or its metal oxides, proved by the EDX and XRD studies; no such secondary phases have been observed. However, the saturation magnetization values of the nanoparticles are found to be 30.2698 emu/g, 32.0148 emu/g, 32.0895 emu/g and 32.9764 emu/g for undoped, 2%, 4% and 6% Co-doped ZnS nanoparticles. The saturation magnetization increases with an increase of Co doping concentration. This suggests that Co-doped ZnS nanoparticles are also responsible for observed paramagnetism. The enhancement in saturation magnetization of Co-doped samples is due to the very small size of Co-doped ZnS nanoparticles. It means that the surface to volume ratio is expected to be very high which further leads to surface defects [41, 42]. In the present study, undoped and Co-doped ZnS nanoparticles exhibited paramagnetism due to small crystallite size and Co doping concentration.

4 Conclusions

Undoped and Co-doped ZnS nanoparticles were prepared at room temperature by the co-precipitation method. XRD studies show that all the nanoparticles are polycrystalline ZnS with a cubic structure. The absence of impurity peaks confirms the prepared nanoparticles are single phase. The reduction in the volume of the unit cell of Co-doped ZnS nanoparticles was observed, which indicates that Co^{2+} ion is incorporated into the ZnS lattice. The average crystallite size of prepared samples was found in the range of 2–3 nm. FE-SEM images of Co-doped nanoparticles showed high agglomeration among
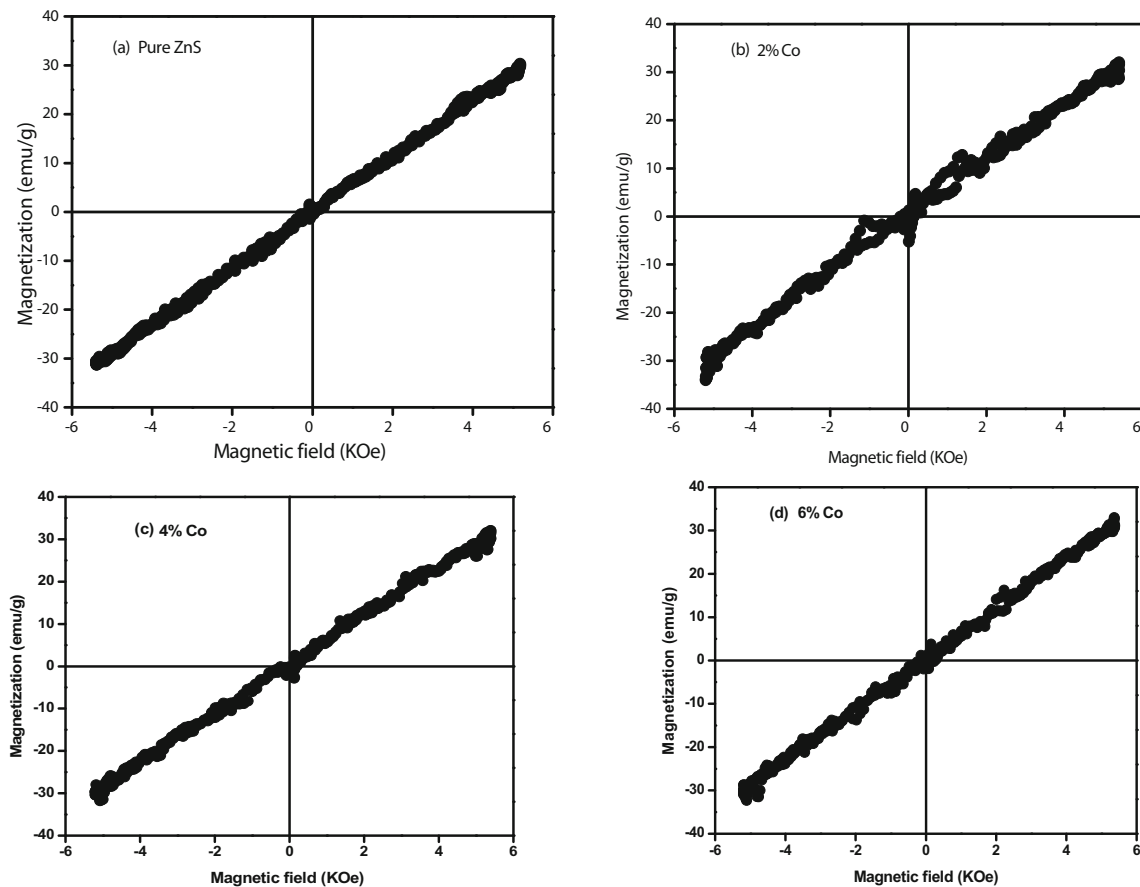
Fig. 9 Magnetization versus applied magnetic field graphs of $Zn_{1-x}Co_xS$ nanoparticles

smaller crystallites to form grains increases with increasing in Co doping concentration. The bandgap of pure ZnS nanoparticles was found to be 3.33 eV, which was found to be red-shifted with the increased Co concentrations. Room temperature paramagnetism arises in undoped and Co-doped ZnS nanoparticles due to small crystallite size and Co doping concentration. Based on the results, the prepared nanoparticles are promising materials in the optoelectronics and spintronics devices.

References

1. A.P. Alivisatos, Semiconductor clusters nanocrystals and quantum dots. Science **271**, 933–937 (1996)
2. A. Le Donne, S. Kanti Jana, S. Banerjee, S. Basu, S. Binetti, J. Appl. Phys. **113**, 014903 (2013). https://doi.org/10.1063/1.4772668
3. P.D. Amico, A. Calzolari, A. Ruini, A. Catellani, New energy with ZnS: novel applications for a standard transparent compound. Sci. Rep. **7**, 16805 (2017)
4. M. Roushani, M. Shamsipur, H.R. Rajabi, J. Electroanal. Chem. **712**, 19 (2014)
5. B. Hemmateenejad, M. Shamsipur, F. Samari, H.R. Rajabi, J. Iran. Chem. Soc. **12**, 1729 (2015)
6. M. Roushani, M. Mavaei, H.R. Rajabi, J. Mol. Catal. A: Chem. **409**, 102 (2015)
7. A. Reddy, G. Murali, R.P. Vijayalakshmi, B.K. Reddy, Appl. Phys. A **105**, 119–124 (2011)
8. B. Sreenivasulu, S. Venkatramana Reddy, P. Venkateswara Reddy, J. Mater. Sci. (2018). https://doi.org/10.1007/s10854-017-7911-5
9. S. Kar, S. Biswas, J. Phys. Chem. C **112**, 11144 (2008)
10. H.C. Ong, R.P.H. Chang, Appl. Phys. Lett. **79**, 3612 (2001)
11. Y.C. Fang, S.Y. Chu, H.C. Chen, J. Electrochem. Soc. **156**, k55 (2009)
12. S. Ghorai, N. Patra, A. Pal, D. Bhattacharya, S.N. Jha, B. Ray, S. Chatterjee, A.K. Ghosh, J. Alloys Compd. **805**, 363–378 (2019)

13. N.K. Sunil Kumar, Verma. J. Mater. Sci. **25**, 1132–1137 (2014)

14. V.D. Mote, Y. Purushotham, B.N. Dole, Cerâmica **59**, 614–619 (2013)

15. Z.L. Wang, Mater Sci Eng R **64**, 33–71 (2009)

16. C. Sociv, A. Zhang, B. Xiang, S.A. Dayeh, D.P.R. Aplin, J. Park, Nano Lett. **7**, 1003–1009 (2007)

17. K. Manzoor, V. Aditya, S.R. Vadera, N. Kumar, T.R.N. Kutty, Solid State Commun. **135**, 16–20 (2005)

18. D. Saikia, J.P. Borah, Appl. Phys. A **124**, 240 (2018)

19. C.S. Pathak, M.K. Mandal, V. Agarwal, Mater. Sci. Semicond. Process. **16**, 467–471 (2013)

20. S. Sambasivam, D.P. Joseph, J.G. Lin, C. Venkateswaran, J. Solid State Chem. **182**, 2598–2601 (2009)

21. S. Kumar, C.L. Chen, C.L. Dong, Y.K. Ho, J.F. Lee, T.S. Chan, R. Thangavel, T.K. Chen, B.H. Mok, S.M. Rao, M.K. Wu, Room J. Alloy. Compd. **554**, 357–362 (2013)

22. N. Eryong, L. Donglai, Z. Yunsen, B. Xue, Y. Liang, J. Yong, J. Zhifeng, S. Xiaosong, Appl. Surf. Sci. **257**, 8762–8766 (2011)

23. C.S. Pathak, M.K. Mandal, Optoelectron. Adv. Mater. Rapid Commun. **5**(3), 211–214 (2011). https://doi.org/10.1007/s10854-014-2287-2

24. J.K. Salem, T.M. Hammad, S. Kuhn, M. Abu Draaz, N.K. Hejazy, R. Hempelmann, J. Mater. Sci. **25**, 2177–2182 (2014). https://doi.org/10.1007/s10854-014-1856-8

25. B.R. Kumar, B. Hymavathi, J. Asian Ceram. Soc. **5**, 94–103 (2017)

26. E. Isbilir, Z. Serbetci, M. Soylu, Superlattice. Microst. **67**, 144–155 (2014)

27. S. Sambasivam, D. Paul Joseph, J.G. Lin, C. Venkateswaran, J. Solid State Chem **182**, 2598 (2009)

28. J. Dai, Z. Jiang, W. Li, G. Bian, Q. Zhu, Mater. Lett. **55**(6), 383–387 (2002)

29. J.F. Reber, K. Meier, J. Phys. Chem. **88**(24), 5903–5913 (1984)

30. D. Saikia, R.D. Raland, J.P. Borah, Phys. E **83**, 56 (2016)

31. B. Poornaprakash, P.T. Poojitha, U. Chalapathi, S. Ramu, R.P. Vijayalakshmi, S.H. Park, Ceram. Int. **42**, 8092 (2016)

32. M.A. Mahadik, Y.M. Hunge, S.S. Shinde, R.Y. Rajpure, G.H. Bhosale, J. Semi. **36**, 033002–33011 (2015)

33. S. Paul, A. Choudhury, Appl. Nanosci. **4**, 839–847 (2014)

34. J. Singh, S. Sharma, S. Soni, S. Sharma, R.C. Singh, Mater. Sci. Semicond. Process. **98**, 29–38 (2019)

35. P.C. Patel, S. Ghosh, P.C. Srivastava, J. Mater. Sci. **50**, 7919–7929 (2015)

36. D. Saikia, J.P. Borah, J Mater Sci **28**, 8029–8037 (2017)

37. S. Elsi, S. Mohanapriya, K. Pushpanathan, J. Supercond. Novel Magn. (2020). https://doi.org/10.1007/s10948-020-05573-4

38. A. Franco Jr., H.V.S. Pessoni, P.R.T. Ribeiro, F.L.A. Machado, J. Magn. Magn. Mater. **426**, 347–350 (2017)

39. C. Bi, L. Pan, M. Xu, L. Qin, J. Yin, Mater. Chem. Phys. **116**, 363–367 (2009)

40. Wu Meirong, Z. Wei, W. Zhao, X. Wang, J. Jiang, J. Nanomateri. **2017**, 1603450 (2017)

41. P. Kaur, S. Kumar, A. Singh, Superlattices Microstruct. **83**, 785–795 (2015)

42. P.K. Sharma, R.K. Dutta, A.C. Pandey, J. Magn. Magn. Mater. **321**, 3457–3461 (2009)